ELSEVIER

Brachytherapy xxx (xxxx) xxx

BRACHYTHERAPY

Dosimetric and workflow impact of synthetic-MRI use in prostate high-dose-rate brachytherapy

Alexander R. Podgorsak[1,*], Bhanu P. Venkatesulu[1], Mohammad Abuhamad[2], Matthew M. Harkenrider[1], Abhishek A. Solanki[1], John C. Roeske[1], Hyejoo Kang[1]

[1] *Department of Radiation Oncology, Stritch School of Medicine, Cardinal Bernardin Cancer Center, Loyola University Chicago, Chicago, IL*
[2] *Department of Computer Science, Loyola University Chicago, Chicago, IL*

ABSTRACT

PURPOSE: Target and organ delineation during prostate high-dose-rate (HDR) brachytherapy treatment planning can be improved by acquiring both a postimplant CT and MRI. However, this leads to a longer treatment delivery workflow and may introduce uncertainties due to anatomical motion between scans. We investigated the dosimetric and workflow impact of MRI synthesized from CT for prostate HDR brachytherapy.

METHODS AND MATERIALS: Seventy-eight CT and T2-weighted MRI datasets from patients treated with prostate HDR brachytherapy at our institution were retrospectively collected to train and validate our deep-learning-based image-synthesis method. Synthetic MRI was assessed against real MRI using the dice similarity coefficient (DSC) between prostate contours drawn using both image sets. The DSC between the same observer's synthetic and real MRI prostate contours was compared with the DSC between two different observers' real MRI prostate contours. New treatment plans were generated targeting the synthetic MRI-defined prostate and compared with the clinically delivered plans using target coverage and dose to critical organs.

RESULTS: Variability between the same observer's prostate contours from synthetic and real MRI was not significantly different from the variability between different observer's prostate contours on real MRI. Synthetic MRI-planned target coverage was not significantly different from that of the clinically delivered plans. There were no increases above organ institutional dose constraints in the synthetic MRI plans.

CONCLUSIONS: We developed and validated a method for synthesizing MRI from CT for prostate HDR brachytherapy treatment planning. Synthetic MRI use may lead to a workflow advantage and removal of CT-to-MRI registration uncertainty without loss of information needed for target delineation and treatment planning. © 2023 American Brachytherapy Society. Published by Elsevier Inc. All rights reserved.

Keywords: Synthetic MRI; Prostate interstitial brachytherapy; Machine learning; Artificial intelligence

Introduction

High-dose-rate (HDR) brachytherapy is an established (1,2) modality for delivering radiation therapy to treat prostate cancer. Prostate HDR brachytherapy results in local control and acceptable bladder and rectum toxicity as either monotherapy (3) for low- or favorable intermediate-risk prostate cancer or as a boost (4) following external beam radiation therapy for unfavorable intermediate- or high-risk disease. Prostate HDR brachytherapy is delivered through interstitial catheters implanted temporarily inside of the prostate under trans-rectal ultrasound guidance. These catheters guide an iridium-192 source to different prostatic regions, allowing a prescription dose of radiation coverage of either the entire prostate gland or a specific focal target (5). To ensure that the catheters are positioned correctly and to enable volumetric treatment planning, the acquisition of a postimplant CT or MRI scans is standard for prostate HDR brachytherapy if ultrasound-based treatment planning is not performed. Generally (6), clinics do not acquire both CT and MRI due to the lengthening of the total procedure time. However, both imaging modalities have unique contributions to planning.

Received 22 November 2022; received in revised form 27 March 2023; accepted 14 May 2023; Available online xxx

* Corresponding author. 2160 S First Avenue, Maywood, IL 60153.
E-mail address: alexander.podgorsak@luhs.org (A.R. Podgorsak).

https://doi.org/10.1016/j.brachy.2023.05.005

Our clinical workflow for prostate HDR brachytherapy combines both CT and MRI. CT is used for identification of the implanted catheters and contouring of the bladder, rectum, and urethra due to its fast acquisition time and low geometric distortion (7). MRI is used to aid in the delineation of the prostate relative to the bladder and rectum (8). Studies (9–14) have suggested that prostate delineation using just CT results in consistently larger volumes than with the aid of MRI, thus increasing dose to surrounding OARs leading to higher toxicity. MRI-based prostate delineation has even led to improved erectile function recovery following treatment (15). To best utilize the information from both scans, an image registration must take place to account for variation in patient positioning between the CT and MRI. Adding uncertainty to this registration process is the patient's internal anatomical changes from the CT to the MRI scan such as bladder or rectal filling. This uncertainty may propagate to the identification of the prostate and surrounding critical structures, which could yield a treatment with increased toxicity or compromised target coverage.

To mitigate these concerns, we propose the generation of synthetic MRI information from the CT scan. This solution would lead to no registration uncertainty necessitating additional margin around structures, as the synthetic image will require no image fusion. This would also enable the use of MRI information to aid in the treatment planning for those unable to undergo the MRI scanning process due to contraindications. Ultimately, this solution would allow for a faster and more efficient brachytherapy treatment workflow because the time and resources needed for the MRI scan would not be required.

Synthesis of MRI data can be carried out using a data-driven framework known as a Generative Adversarial Network (GAN) (16), which combines two types of convolutional neural networks. This artificial intelligence-based method has been successful for image synthesis in the context of radiation oncology (17), being extensively studied in the reverse direction; synthesis of CT information from multiple different MRI sequences (18–20). There have, however, been investigations toward synthetic MRI from CT in anatomical sites like head and neck (21) and the spine (22). These studies have traditionally employed a conditional GAN architecture referred to as Pix2Pix (P2P) (23), which is a combination of a U-net (24) generator with a PatchGAN (25) image classifier for the discriminator. Other works have utilized a GAN architecture called CycleGAN (26) for the task of MRI synthesis for lung (27,28) and brain (29).

The effectiveness of these GAN architectures in certain anatomical sites has been reported, but there are characteristics of the CT and MRI acquisitions in the pelvis which render these "off-the-shelf" architectures not as effective. These are the same characteristics which make image registration between the CT and MRI scan difficult in the first place; variation in external patient positioning and bladder or rectum filling from the time of CT to the time of MRI. P2P-based architectures struggle (30) to learn the mapping from one image to another in the absence of perfectly paired data due to a lacking of proper constraints on the task. Organ filling between images can lead to such a situation. CycleGAN with its unsupervised training cycles can better handle this mismatch, but can (31,32) introduce artificial features into synthetic image data. It is for these reasons that a novel architecture, PCGAN, was developed by our group. PCGAN is a hybrid of P2P and CycleGAN. A separate study is being conducted regarding the image quality of synthetic MRI from PCGAN.

The objective of this study was to evaluate the dosimetric and workflow impact of the use of synthetic MRI from PCGAN in prostate HDR brachytherapy, such that a better understanding of the clinical impact of synthetic MRI could be determined.

Methods and materials

Patient data collection and preprocessing

Postimplant CT & T2-weighted MRI datasets from 95 consecutive prostate HDR brachytherapy treatments delivered at our institution between April 2018 and December 2020 were retrospectively gathered with approval of our institutional review board. Of these 95, seven did not undergo MRI scanning due to contraindications which precluded them from the MRI. Following removal of 10 further image datasets which had severe artifacts on either the CT or MRI scan, the entire dataset consisted of 78 patients. Examples of artifacts which led to image dataset removal from our training dataset were severe metal artifacts on the CT from implanted orthopedic devices or previous low-dose-rate prostate seed implantation, or CT/MRI scans impacted by motion artifacts. Each dataset is comprised of a CT and MRI volume acquired following implantation of the interstitial catheters into the prostate in preparation for HDR brachytherapy. CT data were from a Brilliance Big Bore CT scanner (Philips Health Care, Cleveland OH) using an imaging technique with 140 kVp, 351 mAs, and 2 mm slice thickness. MRI data were from one of two 1.5 T MRI scanners (GE HealthCare, Milwaukee, WI), prior to 2020 was on a Signa HDxt, and from 2020 onward on a Signa Artist. Regardless of the scanner, the T2-weighted axial image data were acquired using a fast spin echo pulse sequence with TR between 4300 ms and 5000 ms depending on the axial field-of-view (FOV), TE of 100 ms, and 3 mm slice thickness.

The preprocessing of this data prior to PCGAN training involved a resampling of the CT data to match the MRI data array size and resolution in all three directions. This step was performed within Velocity oncology imaging informatics system (Varian Medical Systems, Palo Alto, CA). Further preprocessing of the dataset included intensity normalization of the pixel values between 0 and 1.

Please cite this article as: A.R. Podgorsak *et al.*, Dosimetric and workflow impact of synthetic-MRI use in prostate high-dose-rate brachytherapy, Brachytherapy, https://doi.org/10.1016/j.brachy.2023.05.005

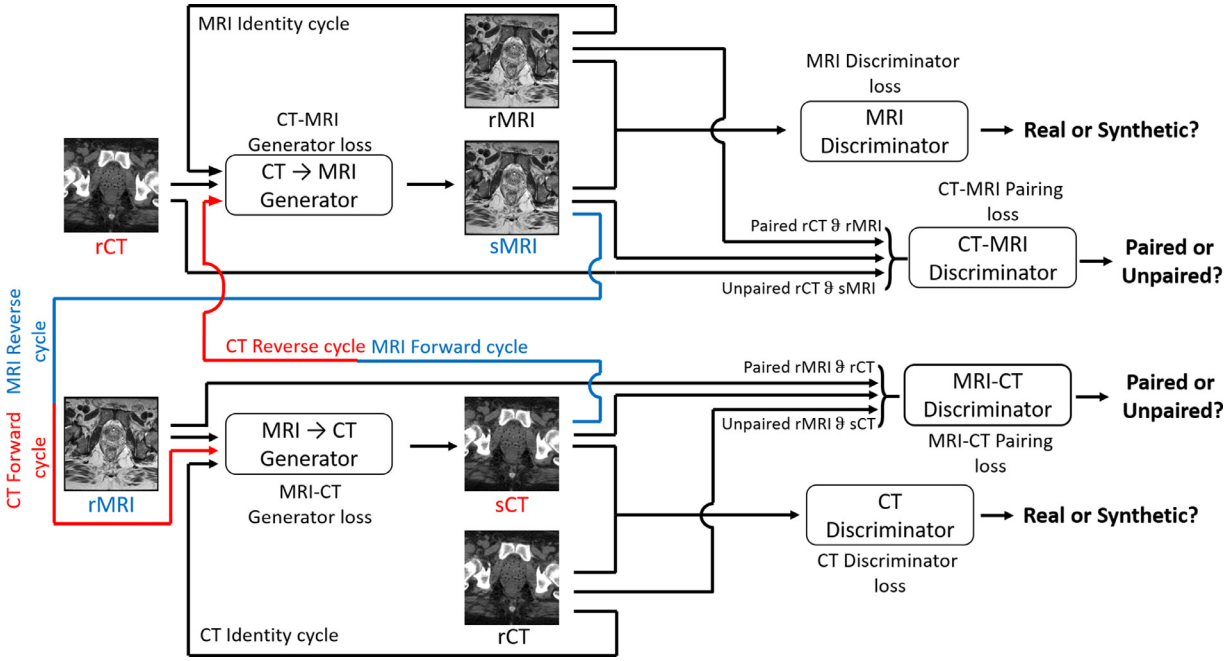

Fig. 1. Flow chart of PCGAN detailing how image data passes between the two generators and four discriminators. Arrows indicate inputs or outputs to or from the generators or discriminators. Color of the text and arrows indicate images used in both the forward and reverse cycle. The two generators have encoder-decoder structure, the four discriminators each have encoder structures.

A deformable registration is not used during this workflow as it is not clinically commissioned at our institution. Fig. 1 details our GAN architecture, PCGAN, tasked with synthesizing axial T2-weighted MRI slices from input axial pelvis CT slices. The idea behind PCGAN is to take advantage of the large regions of the image data which have spatial agreement, generally everywhere but the skin surface, bladder, and rectum, using components of a P2P-based GAN and combine it with transformation cycles classically seen in CycleGAN to account for organ filling and body surface mismatches between the CT and MRI. In this way, we use the strengths of both P2P and CycleGAN while mitigating their weaknesses often seen (33) when certain medical imaging tasks are posed to them. These weaknesses include P2P's requirement for paired training images, and CycleGan's weakness for object transfiguration (34). PCGAN is made up of two encoder-decoder structured generators and four discriminators. The generators consist of an encoder of three convolutional layers followed by 15 ResNet (35) blocks and a decoder of three transposed convolutional layers. There are generators for each domain translation direction, CT to MRI and MRI to CT, with transformation cycles between each generator similar to a CycleGAN. Novel to PCGAN is the use of two discriminators for each generator, one to determine if a synthesized image is real or fake like a standard GAN discriminator, and one to determine if the CT/MRI images posed to the discriminator are paired or unpaired. The combination of these two discriminators adds additional constraints to the task of synthetic MRI generation which helps control the introduction of artificial features into the synthesized images.

Each loss component is given a multiplicative weight based on its ultimate importance toward the overall training process. The weighted generator and discriminator components are all summed to form the total generator and discriminator loss which is minimized during training. During the network development portion of this project, different weighting combinations were attempted which made the contributions of each loss component equal or had one dominant over the other, and a qualitative assessment of the network output was used to judge the weighting effect on the synthesized images. For the clinical context of prostate HDR brachytherapy, we empirically weighted the CycleGAN portion of PCGAN 1.5-times higher than the P2P portion to account for the organ filling and surface mismatches that were observed in our collected dataset, while maintaining enough P2P strength to enforce consistency through the forward and reverse cycles and prevent artificial feature generation.

Training and model validation

Our 78 datasets were pseudo-randomly divided into a training cohort for network development and testing cohort held out from training for quantitative network assessment. This split was done dataset by dataset, not slice by slice so there were no instances where axial slices from the same dataset were present in both the training and testing cohort. Additionally, as there were some datasets from the same

Please cite this article as: A.R. Podgorsak *et al.*, Dosimetric and workflow impact of synthetic-MRI use in prostate high-dose-rate brachytherapy, Brachytherapy, https://doi.org/10.1016/j.brachy.2023.05.005

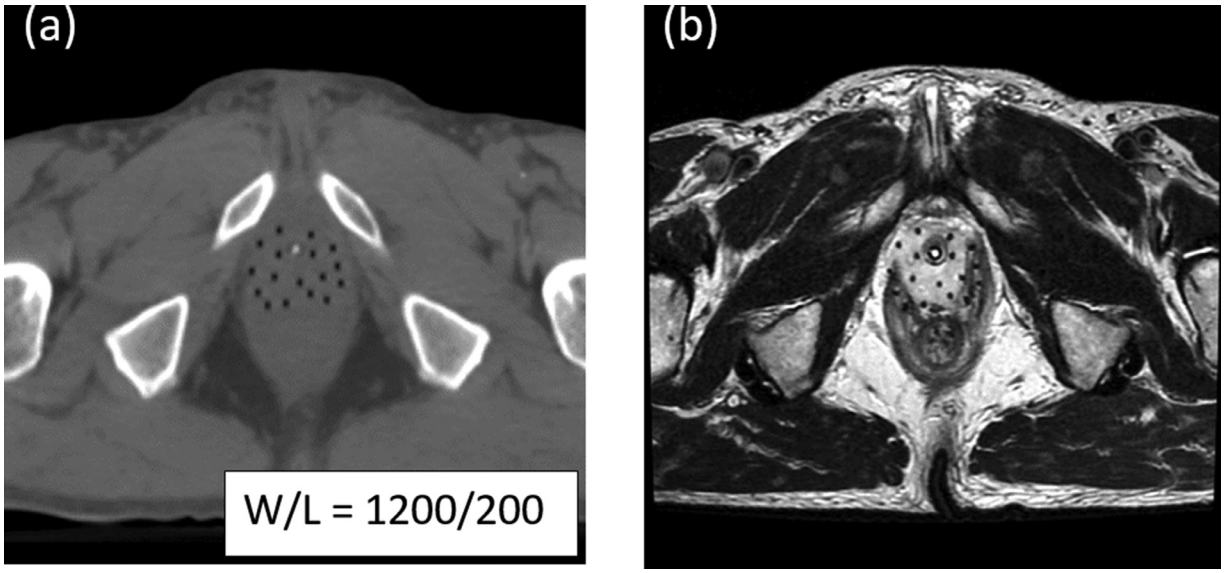

Fig. 2. (a) Example input prostate HDR brachytherapy CT slice with display window/level, and (b) the corresponding ground truth T2-weighted MRI slice. Both images used to train PCGAN for the task of T2-weighted MRI synthesis from a pelvis CT.

patient, care was taken to not have any datasets from the same patient be on opposite sides of the training-testing data split. In the end, the training cohort had 58 patient datasets (number of axial slices = 2216) and the testing cohort had 20 patient datasets (number of axial slices = 785). An example of a CT and MRI pair used for network training is found in Fig. 2.

Network weights were initialized with Glorot weight initialization (36) and updated with the Adam optimizer (37) using hyper-parameters $\beta_1 = 0.5$, $\beta_2 = 0.999$, $\varepsilon = 1E\text{-}7$, and a learning rate of 1E-4. Training was performed using a single Quadro (NVIDIA Corporation, Santa Clara, CA) RTX 6000 graphics processing unit using a batch size of one. GANs can be unstable (38) as they train and may start to synthesize worse images if they are trained for too long. As they lack a unified objective function, an effective method for performance analysis of the GAN output along model training is a visual inspection of the output from validation samples (39) for assessment of the prostate boundary delineation. Training took approximately 6 days to complete the 100 epochs necessary to synthesize MRI images of acceptable quality.

Synthetic MRI evaluation

Following network training, the 20 CT datasets in our testing cohort were used to generate synthetic MRI data which were compared with the ground truth real MRI data in two ways. The prostate was first contoured on Eclipse (Varian Medical Systems, Palo Alto, CA) using both the synthetic and real MRI datasets by a radiation oncologist not originally involved with the clinically delivered plan. Synthetic and real MRI contours were then exported to Velocity and used to compute the dice similarity coefficient (DSC) (40,41) and the mean surface distance (MSD) (42) between the groups. A comparison of these contours using these metrics yields the intermodality variability of prostate segmentation between synthetic and real MRI. The inter-observer variability of prostate segmentation with real MRI was assessed via a comparison between the physician's real MRI contours from this study with the prostates contoured during the clinically delivered plan using real MRI by one of two other radiation oncologists. In this way, the intermodality variability between real and synthetic MRI was compared with the inter-observer variability of prostate segmentation on real MRI. The statistical significance of any difference was assessed via a Student's single-tailed heteroscedastic *t*-test (43) using a significance threshold of 0.05.

The prostate structure on real and synthetic MRI was then used to create new planning target volumes (PTVs) with an isotropic 3 mm expansion followed by removal of the urethra, bladder, and rectum. Adjustment of the source dwell times in the original CT-defined clinically delivered catheter positions was performed to re-plan the brachytherapy treatment to cover the synthetic MRI PTV with the prescription dose (either 13.5 Gy for two fractions for monotherapy or 15 Gy for a single fraction boost) in a manner consistent with the originally delivered treatment in terms of target coverage and dose to the surrounding critical structures. This new dose was then overlaid onto the real MRI PTV. The dosimetric impact of using the synthetic MRI for planning was assessed by a comparison of dose volume histogram (DVH) metrics such as PTV $V_{100\%}$, $V_{150\%}$, and $V_{200\%}$ (PTV receiving 100%, 150%, and 200% of the prescription dose respectively) averaged over all 20 datasets in our test cohort. Additionally, the dose to the surrounding OARs in the synthetic MRI PTV-targeted

Please cite this article as: A.R. Podgorsak *et al.*, Dosimetric and workflow impact of synthetic-MRI use in prostate high-dose-rate brachytherapy, Brachytherapy, https://doi.org/10.1016/j.brachy.2023.05.005

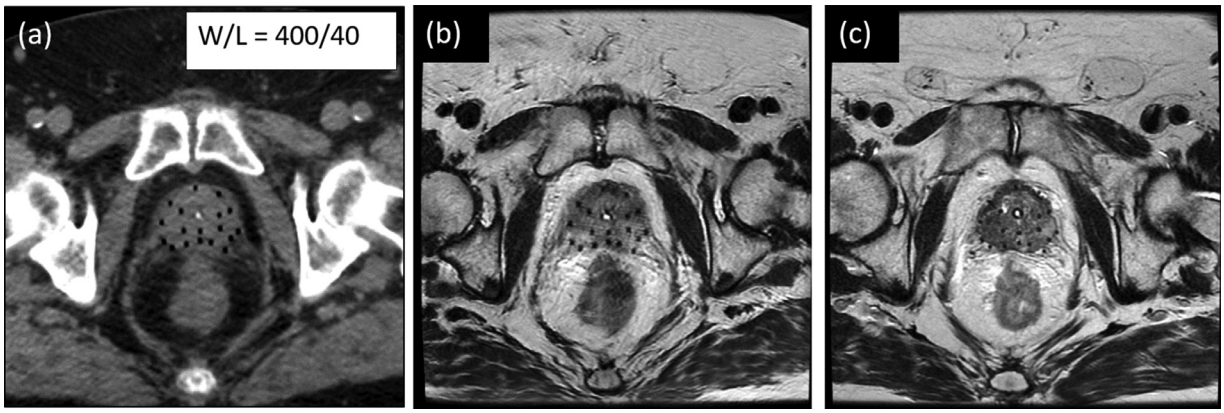

Fig. 3. (a) Example prostate HDR brachytherapy CT slice from the testing cohort with display window/level, (b) corresponding synthetic MRI output from trained PCGAN, (c) ground truth MRI scan indicating qualitative agreement between it and the network output in (b).

treatments was compared with the clinically delivered plan using D_{1cc} (minimum dose received by maximally irradiated 1 cubic centimeter of the considered structure) for the bladder, rectum, and urethra averaged over all 20 datasets in our test cohort. Because there were different prescription doses present in our testing cohort depending on if the brachytherapy treatment was used as monotherapy or as an external beam boost, we report D_{1cc} as a percentage of the prescription dose. In this way, DVH metrics from plans targeting the synthetic MRI PTV were compared with plans targeting the real MRI PTV such that we assessed how delivering dose to the synthetic MRI-defined PTV would cover the "ground truth" real MRI-defined PTV and how it would impact the surrounding critical organs relative to the clinically delivered original treatment plans.

Results

Qualitative assessment of synthetic MRI

Fig. 3 shows a CT slice from the testing cohort, synthetic T2-weighted MRI from our trained PCGAN, and corresponding ground truth T2-weighted MRI. There is visual similarity between the synthetic and real MRI across the lateral extent of the prostate and posteriorly toward the rectum. The slight mis-registration between the ground truth CT and MRI is also apparent, showing a weakness of rigid body registration between the CT and real MRI and the need for deformable image registration moving forward. Fig. 4 shows a synthetic as well as a real coronal and sagittal MRI slice for the same patient shown in Fig. 3. There is qualitative agreement between the synthetic and real MRI extending from the prostate apex to the base.

Intermodality vs interobserver variability of prostate contours

A box and whisker plot which details the DSC and MSD between prostate contours from synthetic MRI and real MRI (intermodality, blue), and the DSC and MSD between prostate contours from the observer in this study and the contour from the clinically delivered treatment (interobserver, pink) averaged over the 20 datasets in the test cohort can be found in Figs. 5a and b, respectively. The inter-modality variability of the prostate contour between synthetic and real MRI was found to be statistically similar (DSC $p = 0.37$, MSD $p = 0.47$) to the inter-observer variability of the prostate contour between observers.

Dosimetric impact of synthetic MRI

Fig. 6 shows an axial, coronal, and sagittal CT slice of the prostate with the real and synthetic MRI PTV overlaid along with the 100% prescription isodose line from a representative patient in the testing cohort. There are comparable contours and target coverage between the real and synthetic MRI PTV in this slice, extending throughout the entire volume from the apex to the base. Fig. 7 shows box and whisker plots detailing the variation of PTV $V_{100\%}$, $V_{150\%}$, and $V_{200\%}$ for the synthetic and real MRI datasets within the test cohort. Re-planning the original treatment to cover the synthetic MRI PTV led to all three constraints being met on both the synthetic and real MRI PTV structures, and no statistical difference between the three DVH metrics considering the synthetic and real MRI PTV. Box and whisker plots showing the variation of D_{1cc} for the bladder, rectum, and urethra for the synthetic MRI PTV plans and the clinically delivered real MRI plans in the test cohort can be found in Fig. 8. While there were increases in bladder, rectum, and urethra doses in the plans targeting the synthetic MRI PTV compared with the clinically delivered plans, in no case did this lead to an increase above the institutional organ dose constraint for D_{1cc}. Included in the Figs. 7 and 8 with the dashed black lines are institutional target goals and OAR dose constraints based on American Brachytherapy Society guidance (1). A smaller range of OAR doses was observed in the synthetic MRI-PTV plans compared with the clinically delivered

Please cite this article as: A.R. Podgorsak *et al.*, Dosimetric and workflow impact of synthetic-MRI use in prostate high-dose-rate brachytherapy, Brachytherapy, https://doi.org/10.1016/j.brachy.2023.05.005

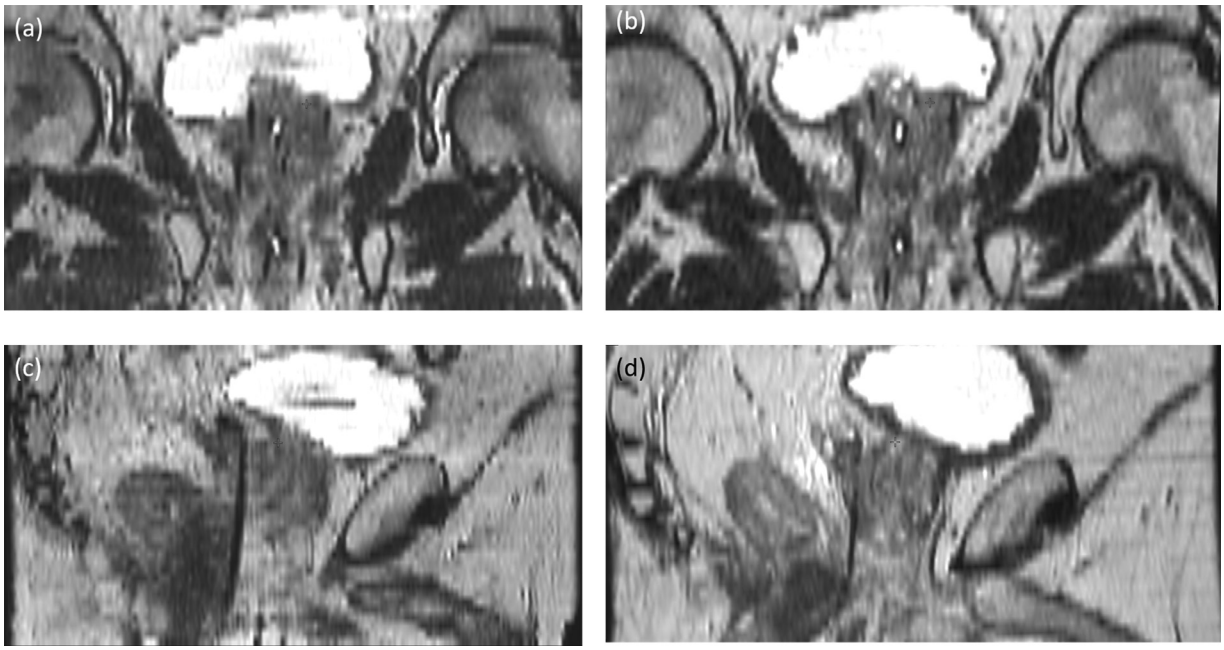

Fig. 4. Synthetic (a) coronal and (c) sagittal MRI and real (b) coronal and (d) sagittal MRI slices of the same patient scan from Fig. 3 showing agreement of the synthetic and real MRI scan at the prostate apex and base.

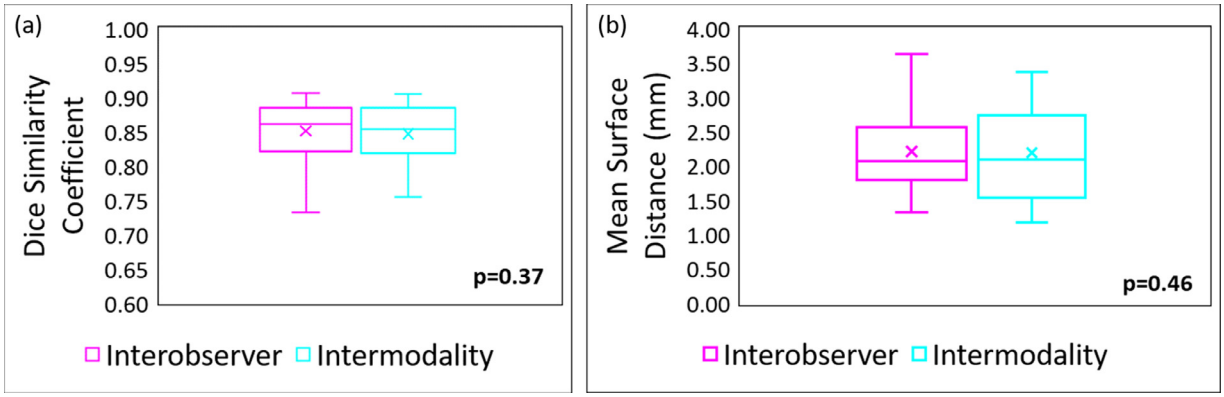

Fig. 5. Box and whisker plots of the (a) dice similarity coefficient and (b) mean surface distance between prostate contours drawn on real and synthetic MRI (intermodality, blue, right) and those between prostate contours drawn on real MRI by two different observers (interobserver, pink, left). Included on plot are *p*-values between two groups, showing no difference between interobserver and intermodality variability in the prostate contouring process.

plans. This could be attributed to the same individual planning the synthetic MRI-PTV plans, compared to different individuals planning the clinically delivered plans over the two-and-a-half years that this study collected cases over.

Discussion

This aim of this work was to determine the impact of using synthetic MRI at different steps of the prostate HDR brachytherapy delivery workflow. For target delineation, we found minimal differences between prostate contours drawn on real and synthetic MRI. Dosimetrically, target coverage was no different between using real or synthetic MRI to plan. Finally, there were no violations of institutional dose constraints for urethra, bladder and rectum when planning with the synthetic MRI.

Geometric variability of the prostate contour was assessed using the DSC and MSD between prostate contours drawn on synthetic MRI and those from real MRI by the same observer, and compared this value with the DSC and MSD between different observers' prostate contour drawn on the same real MRI scan. Following this, the dosimetric impact on a real MRI PTV by planning a prostate HDR brachytherapy treatment to target the synthetic MRI PTV was assessed via DVH metrics such as PTV $V_{100\%}$, $V_{150\%}$, and $V_{200\%}$. The impact on the surrounding critical structures by the synthetic MRI PTV targeted plans was also assessed using D_{1cc} and compared with the clinically delivered plan.

Please cite this article as: A.R. Podgorsak *et al.*, Dosimetric and workflow impact of synthetic-MRI use in prostate high-dose-rate brachytherapy, Brachytherapy, https://doi.org/10.1016/j.brachy.2023.05.005

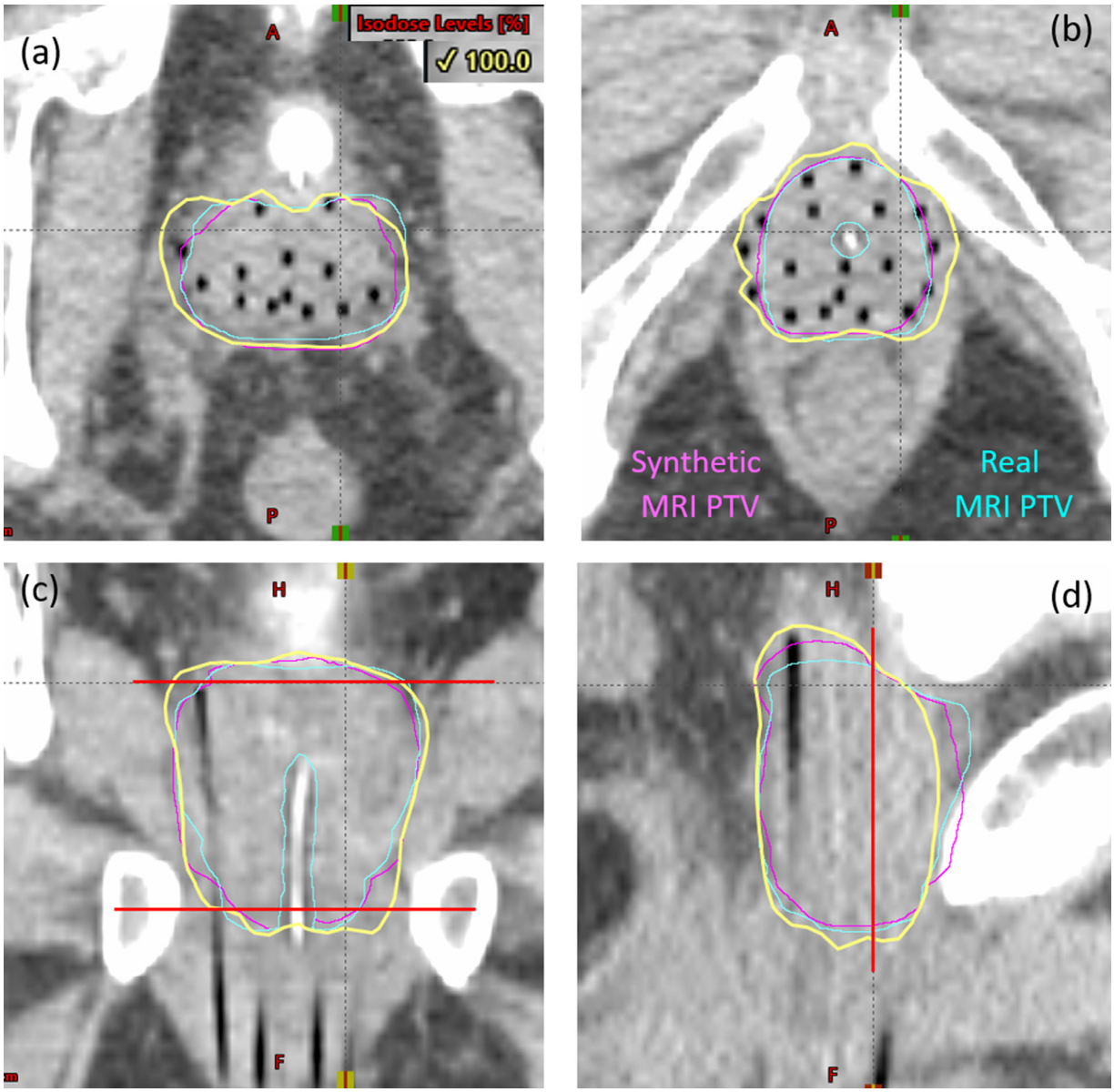

Fig. 6. Axial CT slice of the prostate (a) base and (b) apex from our testing cohort showing real (rMRI, blue) and synthetic (sMRI, pink) planning target volumes expanded from prostate contours and the coverage of the 100% prescription (Rx) isodose line from the re-planning of the HDR brachytherapy treatment. The Rx isodose line covers both targets well in these slices, as well as over the entire volume as seen in the (c) coronal and (d) sagittal slices. Display window/level used was 700/-110. Red lines in (c) indicate location of axial slices at base (a) and apex (b). Red line in (d) indicates location of coronal slice (c).

Averaged over the 20 datasets in the test cohort, the DSC between the real and synthetic MRI prostate contours was (average ± standard deviation) 0.846 ± 0.045, compared with 0.852 ± 0.057 for the DSC between the different observers using the real MRI to draw the prostate contour ($p = 0.37$). Considering the MSD, a similar trend was observed. MSD between the real and synthetic MRI prostate contours was 2.19 ± 0.69 mm, compared with 2.47 ± 0.50 mm for the MSD between the different observers using real MRI ($p = 0.47$). Both geometric results indicate the inter-observer variability of the prostate contour using real MRI is similar to the inter-modality variability of the prostate contour using real or synthetic MRI. This shows how the prostate contour accuracy is not statistically affected through the use of synthetic MRI generated from PCGAN.

PTV DVH metrics indicate no decrease in real MRI-defined target coverage if the synthetic MRI PTV was used to plan, nor any unacceptable increase in the dose hotspots. This is important as a loss in target coverage such that a tumorcidal dose is not delivered can lead to losses in local control in radiotherapy (44). There were increases in

Please cite this article as: A.R. Podgorsak *et al.*, Dosimetric and workflow impact of synthetic-MRI use in prostate high-dose-rate brachytherapy, Brachytherapy, https://doi.org/10.1016/j.brachy.2023.05.005

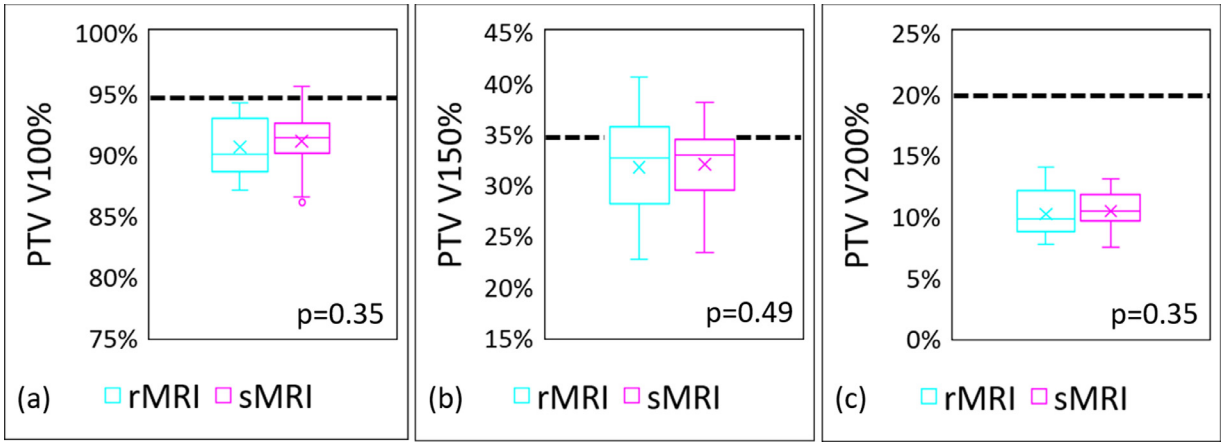

Fig. 7. Box and whisker plots of the re-planning result targeting the synthetic MRI (sMRI) PTV (pink, right), and dose overlaid onto the real MRI (rMRI) PTV (blue, left). (a) $V_{100\%}$, (b) $V_{150\%}$, (c) $V_{200\%}$. Included on the plots are the institutional constraint for target coverage shown in the dashed black line, in terms of percentage of prescription dose.

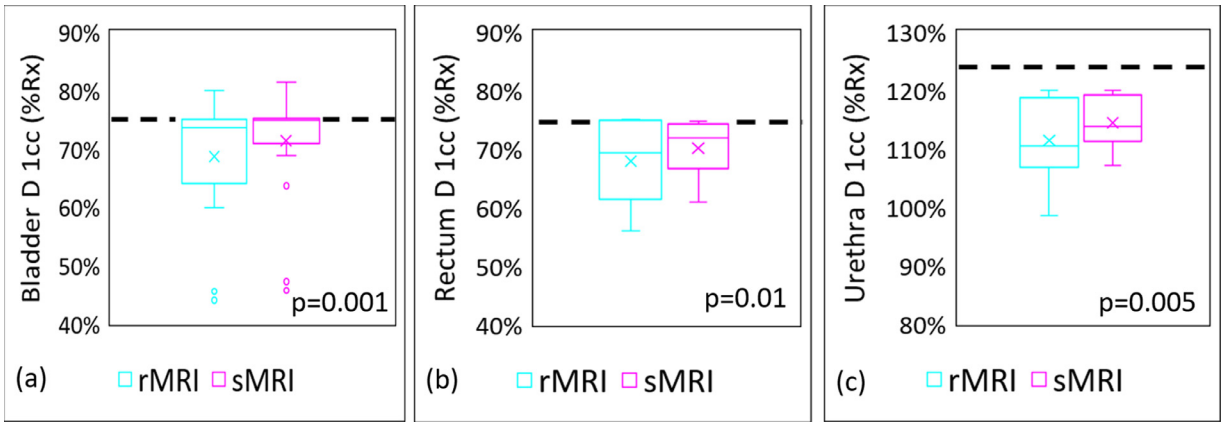

Fig. 8. Box and whisker plots of the re-planning result targeting the synthetic MRI (sMRI) PTV (pink, right), and dose overlaid onto the real MRI (rMRI) bladder, rectum, and urethra. (a) Bladder D_{1cc}, (b) rectum D_{1cc}, (c) urethra D_{1cc}. Included on the plots are the institutional constraint for each organ shown in the dashed black line, in terms of percentage of prescription dose.

the D_{1cc} of the bladder, rectum, and urethra in the synthetic MRI re-planned treatments. These increases can be explained by our use of the original catheter positions for the synthetic MRI re-plans. The synthetic MRI-defined target occasionally extended to regions without any catheter placement. This led to slight increases in some of the peripheral catheter dwell times to ensure proper target coverage, thus increasing dose to the surrounding OARs. It must be noted that this did not lead to an increase above institutional dose constraints. Toxicity to these organs induced by prostate HDR brachytherapy is a major concern. Any increases above the dose constraints in these structures would be unacceptable and necessitate dropping the target coverage, potentially reducing the probability of local disease control.

Lastly, the rapid generation of a synthetic T2-weighted MRI would yield an immediate workflow advantage. A proposed clinical workflow following synthetic MRI implementation is as follows: a patient receives a postimplant pelvis CT scan. Within a few seconds of the CT scan and with the patient still on the scanner table, physicians can review the postimplant CT and synthetic MRI information and begin target and critical structure delineation, on a timescale that is much quicker than the current workflow. Synthetic MRI information could be used to start the planning process before acquisition of the real MRI. The real MRI information could be obtained and registered to the CT and synthetic MRI to confirm the prostate contour. Assuming everything matches, treatment can proceed. Once sufficient institutional confidence in the synthetic MRI is achieved, the real MRI might only be acquired in the case of a poor synthetic MRI generation. This would speed up the treatment planning even more. Synthetic MRI has the potential to greatly accelerate the entire clinical workflow, at no "cost" or loss of clinical information as in the case of skipping the real MRI. We consider synthetic MRI to

Please cite this article as: A.R. Podgorsak *et al.*, Dosimetric and workflow impact of synthetic-MRI use in prostate high-dose-rate brachytherapy, Brachytherapy, https://doi.org/10.1016/j.brachy.2023.05.005

be "free" information. Prostate contours on synthetic MRI were sufficiently accurate such that brachytherapy plans were consistent with the originally treated plan which used the real MRI target. It should be noted that this temporal advantage does not include the time it takes for the image registration between the CT and the real MRI scan. As the synthetic MRI is generated from the CT, it will not require any image fusion prior to use for contouring. These image registrations can be time-consuming, taking on the order of 20–30 minutes to ensure a good-quality match between the CT and real MRI. The workflow advantage may be even greater that what is reported here. The image registration process between CT and MRI also adds additional uncertainty to the target and surrounding critical structure delineation. It is reported (45–49) that uncertainties between 2 and 5 mm are introduced during registration. This error is systematic and could potentially shift high-dose regions away from the target which may compromise tumor control.

An additional note regarding this work is the generalizability of it to other institutions which utilize a CT or combined CT/MRI planning workflow for HDR brachytherapy. Theoretically, one could use this deep-learning-based framework for synthetic MRI generation with just a CT. It is likely that differences in CT vendor, or even acquisition protocol differences would necessitate at least transfer learning to improve the synthetic MRI generation, however this method of image synthesis using clinically paired multi-modality data would be generalizable to any institution with a large enough institutional dataset to train the model.

There has been other work in the space of generating MRI information from CT scans of the male pelvis (50–52), with important differences separating our work from the previously published work in the literature. Firstly, these prior studies used planning CT-simulation scans as the input and diagnostic MRI scans from a different day for MRI synthesis for external beam radiation therapy. We feel that visualization of the intraprostatic detail needed for prostate HDR brachytherapy treatment planning is a more complicated task. Secondly, the previous studies used a pure CycleGAN for image synthesis instead of a custom hybrid network.

There are limitations to this work. Use of DSC provides an estimate as to the overlap between the prostate contours, but ignores where there is not overlap. If the synthetic MRI prostate contour extends closer towards the bladder, rectum, or urethra, this could lead to an increase in toxicity to the patient relative to a target defined using real MRI. While this was not seen when looking at the doses to the surrounding critical structures in the synthetic MRI PTV-target plans, DSC is not sensitive to the location of the discrepancy. Use of MSD helps, but still has certain limitations in that it may not be sensitive to contour outliers which could have dosimetric impact. Furthermore, because our OAR dose comparison did not have PTV target coverage normalized between the clinically delivered and synthetic MRI re-planned cases, the comparison is somewhat clinically based. Seventy-eight unique patient datasets have a low likelihood of containing all of the potential edge cases that our trained network should be robust to for eventual clinical implementation, and work is underway to expand this number. It should be noted though, that our number of collected patient datasets are on a similar scale or greater to those of similar published works for medical image synthesis using a GAN (18,20,53). Lastly, we excluded images from training that contained imaging artifacts. Further investigation will be carried out to determine how the network performs with these data, and how we can extend our network's performance to include these and other edge cases. Lastly, our use of rigid-body registration to fuse the ground truth CT and MRI introduced slight misalignments in our training data. A well-validated deformable image registration process would better account for the internal organ motion which occurs between the time of the CT and MRI, thus may enable more successful algorithm training due to better agreement between the input CT and ground truth MRI. This will be an important part of the future development of work such as these.

Moving forward, there are many avenues where this work can be expanded to. Related to prostate cancer, the F-Sharp trial (5) is an example where an intraprostatic recurrence is treated just to a portion of the prostate, instead of the entire gland. Synthetic MRI could be useful for delineating these lesions. Considering other disease sites, gynecological cancers have long been underrepresented in research. Treatment planning for brachytherapy treatments using a tandem and ovoid/ring (with or without needles) will often include or be based completely on an MRI scan. In patients unable to undergo a real MRI scan or for workflow advantages similar to what was shown during this work, synthetic MRI could be a welcome addition to the clinical workflow for endometrial cancers. Lastly, there are implications of this work in external beam radiation therapy, as MRI is being combined with CT more than ever for treatment planning. Synthetic MRI should show value here as well.

Conclusions

This study demonstrates that PCGAN can synthesize T2-weighted MRI volumes on a timescale that should help accelerate the workflow for prostate HDR brachytherapy without losing the soft-tissue MRI information. There was dosimetric similarity between targeting synthetic MRI defined PTVs and real MRI defined PTVs, without increasing dose to surrounding critical structures beyond institutional dose constraints. With further synthetic MRI image quality improvement, synthetic MRI may become an integrated part of the standard clinical workflow for prostate HDR brachytherapy.

Please cite this article as: A.R. Podgorsak *et al.*, Dosimetric and workflow impact of synthetic-MRI use in prostate high-dose-rate brachytherapy, Brachytherapy, https://doi.org/10.1016/j.brachy.2023.05.005

References

[1] Yamada Y, Rogers L, Demanes DJ, et al. American Brachytherapy Society consensus guidelines for high-dose-rate prostate brachytherapy. *Brachytherapy* 2012;11:20–32.
[2] Harkenrider MM, Albuquerque K, Brown D, et al. ACR–ABS–ASTRO practice parameter for the performance of radionuclide-based high-dose-rate brachytherapy. *Brachytherapy* 2021;20:1071–1082.
[3] Morton G, McGuffin M, Chung HT, et al. Prostate high dose-rate brachytherapy as monotherapy for low and intermediate risk prostate cancer: Efficacy results from a randomized phase II clinical trial of one fraction of 19 Gy or two fractions of 13.5 Gy. *Radiother Oncol* 2020;146:90–96.
[4] Wedde TB, Smastuen MC, Brabrand S, et al. Ten-year survival after high-dose-rate brachytherapy combined with external beam radiation therapy in high-risk prostate cancer: A comparison with the Norwegian SPCG-7 cohort. *Radiother Oncol* 2019;132:211–217.
[5] Solanki AA, Adams W, Baldea K, et al. "A multi-institutional phase I/II trial of focal salvage high-dose-rate brachytherapy for locally recurrent prostate cancer in patients treated with prior radiotherapy (F-SHARP)." (2021): TPS265.
[6] Krauss DJ. High dose rate brachytherapy for prostate cancer: Current techniques and applications to varying disease presentations. *Appl Rad Oncol* 2017;6:12–17.
[7] Yang X, Rossi P, Ogunleye T, et al. Prostate CT segmentation method based on nonrigid registration in ultrasound-guided CT-based HDR prostate brachytherapy. *Med Phys* 2014;41:111915.
[8] Blanchard P, Ménard C, Frank SJ. Clinical use of magnetic resonance imaging across the prostate brachytherapy workflow. *Brachytherapy* 2017;16:734–742.
[9] Roach III M, Faillace-Akazawa P, Malfatti C, et al. Prostate volumes defined by magnetic resonance imaging and computerized tomographic scans for three-dimensional conformal radiotherapy. *Int J Radiat Oncol Biol Phys* 1996;35:1011–1018.
[10] Dinh CV, Steenbergen P, Ghobadi G, et al. Magnetic resonance imaging for prostate cancer radiotherapy. *Phys Med* 2016;32:446–451.
[11] Crook J, Marbán M, Batchelar D. HDR prostate brachytherapy. Seminars in radiation oncology, 30. WB Saunders; 2020. p. 49–60.
[12] Smith WL, Lewis C, Bauman G, et al. Prostate volume contouring: A 3D analysis of segmentation using 3DTRUS, CT, and MR. *Int J Radiat Oncol Biol Phys* 2007;67:1238–1247.
[13] Villeirs GM, Vaerenbergh KV, Vakaet L, et al. Interobserver delineation variation using CT versus combined CT+ MRI in intensity-modulated radiotherapy for prostate cancer. *Strahlenther Onkol* 2005;181:424–430.
[14] Rasch C, Barillot I, Remeijer P, et al. Definition of the prostate in CT and MRI: A multi-observer study. *Int J Radiat Oncol Biol Phys* 1999;43:57–66.
[15] Harris AA, Wu M, Deirmenjian JM, et al. Computed tomography versus magnetic resonance imaging in high-dose-rate prostate brachytherapy planning: The impact on patient-reported health-related quality of life. *Brachytherapy* 2021;20:66–74.
[16] Goodfellow I, Pouget-Abadie J, Mirza M, et al. Generative adversarial networks. *Commun ACM* 2020;63:139–144.
[17] Kawahara D, Ozawa S, Kimura T, Nagata Y. Image synthesis of monoenergetic CT image in dual-energy CT using kilovoltage CT with deep convolutional generative adversarial networks. *J Appl Clin Med Phys* 2021;22:184–192.
[18] Liu X, Emami H, Nejad-Davarani SP, et al. Performance of deep learning synthetic CTs for MR-only brain radiation therapy. *J Appl Clin Med Phys* 2021;22:308–317.
[19] Hsu S-H, DuPre P, Peng Q, Tome WA. A technique to generate synthetic CT from MRI for abdominal radiotherapy. *J Appl Clin Med Phys* 2020;21:136–143.
[20] Tang B, Wu F, Fu W, et al. Dosimetric evaluation of synthetic CT image generated using a neural network for MR-only brain radiotherapy. *J Appl Clin Med Phys* 2021;22:55–62.
[21] Kieselmann JP, Fuller CD, Gurney-Champion OJ, Oelfke U. Cross–modality deep learning: Contouring of MRI data from annotated CT data only. *Med Phys* 2021;48:1673–1684.
[22] Jin C-B, Kim H, Liu M, et al. DC2Anet: Generating lumbar spine MR images from CT scan data based on semi-supervised learning. *Appl Sci* 2019;9:2521.
[23] Isola P, Zhu J-Y, Zhou T, Efros AA. Image-to-image translation with conditional adversarial networks. In: Proceedings of the IEEE conference on computer vision and pattern recognition; 2017.
[24] Ronneberger O, Fischer P, Brox T. U-net: Convolutional networks for biomedical image segmentation. In: International conference on medical image computing and computer-assisted intervention, Cham. Springer; 2015.
[25] Li C, Wand M. Precomputed real-time texture synthesis with Markovian generative adversarial networks. In: European conference on computer vision. Cham: Springer; 2016.
[26] Zhu J-Y, Park T, Isola P, Efros AA. Unpaired image-to-image translation using cycle-consistent adversarial networks. In: Proceedings of the IEEE international conference on computer vision; 2017.
[27] Jiang J, Hu Y-C, Tyagi N, et al. Tumor-aware, adversarial domain adaptation from CT to MRI for lung cancer segmentation. In: International conference on medical image computing and computer-assisted intervention, Cham. Springer; 2018.
[28] Jiang J, Hu Y-C, Tyagi N, et al. Cross-modality (CT-MRI) prior augmented deep learning for robust lung tumor segmentation from small MR datasets. *Med Phys* 2019;46:4392–4404.
[29] Jin C-B, Kim H, Liu M, et al. Deep CT to MR synthesis using paired and unpaired data. *Sensors* 2019;19:2361.
[30] Tripathy S, Kannala J, Rahtu E. Learning image-to-image translation using paired and unpaired training samples. In: Asian conference on computer vision, Cham. Springer; 2018.
[31] Cohen JP, Luck M, Honari S. Distribution matching losses can hallucinate features in medical image translation. In: International conference on medical image computing and computer-assisted intervention, Cham. Springer; 2018.
[32] Kang E, Koo HJ, Yang DH, et al. Cycle-consistent adversarial denoising network for multiphase coronary CT angiography. *Med Phys* 2019;46:550–562.
[33] Singh NK, and Raza K. "Medical image generation using generative adversarial networks: A review." Health informatics: a computational perspective in healthcare (2021): 77-96.
[34] Zhou S, Xiao T, Yang Y, et al. Genegan: learning object transfiguration and attribute subspace from unpaired data, 2017. arXiv preprint arXiv: 1705.04932.
[35] He K, Zhang X, Ren S, Sun J. Deep residual learning for image recognition. In: Proceedings of the IEEE conference on computer vision and pattern recognition; 2016.
[36] Glorot X, Bengio Y. Understanding the difficulty of training deep feedforward neural networks. In: *Proceedings of the thirteenth international conference on artificial intelligence and statistics*. JMLR Workshop and Conference Proceedings; 2010.
[37] Kingma DP, Ba J. Adam: a method for stochastic optimization, 2014. arXiv preprint arXiv: 1412.6980.
[38] Mescheder L, Geiger A, Nowozin S. Which training methods for GANs do actually converge?. In: International conference on machine learning. PMLR; 2018.
[39] Salimans T, Goodfellow I, Zaremba W, et al. Improved techniques for training gans. *Adv Neural Inf Process Syst* 2016;29.
[40] Sorensen T. A method of establishing groups of equal amplitude in plant sociology based on similarity of species content and its application to analyses of the vegetation on Danish commons. *Biol Skar* 1948;5:1–34.
[41] Dice LR. Measures of the amount of ecologic association between species. *Ecology* 1945;26:297–302.

Please cite this article as: A.R. Podgorsak *et al.*, Dosimetric and workflow impact of synthetic-MRI use in prostate high-dose-rate brachytherapy, Brachytherapy, https://doi.org/10.1016/j.brachy.2023.05.005

[42] Rockafellar RT, Wets RJ-B. Variational analysis, Vol. 317. Springer Science & Business Media, 2009.
[43] Student The probable error of a mean. *Biometrika* 1908;6:1–25.
[44] Shaverdian N, Tenn S, Veruttipong D, et al. The significance of PTV dose coverage on cancer control outcomes in early stage non-small cell lung cancer patients treated with highly ablative stereotactic body radiation therapy. *Br J Radiol* 2016;89:20150963.
[45] Van Herk M, Kooy HM. Automatic three-dimensional correlation of CT-CT, CT-MRI, and CT-SPECT using chamfer matching. *Med Phys* 1994;21:1163–1178.
[46] Ulin K, Urie MM, Cherlow JM. Results of a multi-institutional benchmark test for cranial CT/MR image registration. *Int J Radiat Oncol Biol Phys* 2010;77:1584–1589.
[47] Dean CJ, Sykes JR, Cooper RA, et al. An evaluation of four CT–MRI co-registration techniques for radiotherapy treatment planning of prone rectal cancer patients. *Br J Radiol* 2012;85:61–68.
[48] Korsager AS, Carl J, Østergaard LR. Comparison of manual and automatic MR-CT registration for radiotherapy of prostate cancer. *J Appl Clin Med Phys* 2016;17:294–303.
[49] Brock KKDeformable Registration Accuracy Consortium. Results of a multi-institution deformable registration accuracy study (MIDRAS). *Int J Radiat Oncol Biol Phys* 2010;76:583–596.
[50] Dong X, Lei Y, Tian S, et al. Synthetic MRI-aided multi-organ segmentation on make pelvic CT using cycle consistent deep attention network. *Radiother Oncol* 2019;141:192–199.
[51] Lei Y, Dong X, Tian Z, et al. CT prostate segmentation based on synthetic MRI-aided deep attention fully convolution network. *Med Phys* 2020;47:530–540.
[52] Lei Y, Wang T, Tian S, et al. Male pelvic CT multi-organ segmentation using synthetic MRI-aided dual pyramid networks. *Phys Med Biol* 2021;66.
[53] Kazemifar S, Barragan Montero AM, Souris K, et al. Dosimetric evaluation of synthetic CT generated with GANs for MRI-only proton therapy treatment planning of brain tumors. *J Appl Clin Med Phys* 2020;21:76–86.

Please cite this article as: A.R. Podgorsak *et al.*, Dosimetric and workflow impact of synthetic-MRI use in prostate high-dose-rate brachytherapy, Brachytherapy, https://doi.org/10.1016/j.brachy.2023.05.005